PERGAMON

International Journal of Solids and Structures 40 (2003) 2645–2658

INTERNATIONAL JOURNAL OF SOLIDS and STRUCTURES

www.elsevier.com/locate/ijsolstr

Boundary element modeling for defect characterization potential in a wave guide

Xiaoliang "George" Zhao, Joseph L. Rose *

Department of Engineering Science and Mechanics, The Pennsylvania State University, 212 Earth-Engineering Science Building, University Park, PA 16802, USA

Received 14 November 2002; received in revised form 14 January 2003

Abstract

Wave scattering analysis implemented by boundary element methods (BEM) and the normal mode expansion technique is used to study the sizing potential of two-dimensional shaped defects in a wave guide. Surface breaking half-elliptical shaped defects of three opening lengths (0.3, 6.35 and 12.7 mm) and through-wall depths of 10–90% on a 10 mm thick steel plate were considered. The reflection and transmission coefficients of both Lamb and shear horizontal (SH) waves over a frequency range 0.05–2 MHz were studied. A powerfully practical result was obtained whereby the numerical results for the S_0 mode Lamb wave and n_0 mode SH wave at low frequencies showed a monotonic increase in signal amplitude with an increase in the defect through-wall depth. At high frequency (usually above the cut-off frequency of the A_1 mode for Lamb waves and the n_1 mode for SH waves, respectively), the monotonic trend does not hold in general due to the energy redistribution to the higher order wave modes. Guided waves impinging onto an internal stringer-like an inclusion were also studied. Both the Lamb and SH waves were shown to be insensitive to the stringer internal inclusions at low frequency. Experiments with piezoelectric Lamb wave transducers and non-contact SH wave electro-magnetic acoustic transducers (EMAT) verified some of the theoretical results.

Keywords: Boundary element methods; Guided waves; Wave scattering; Shear horizontal waves; Lamb waves; Defect sizing

1. Introduction

Pipelines in the gas industry are aging. Inspection systems are needed to locate defects and to be able to characterize and size them efficiently. Existing technologies for pipe inspection such as magnetic flux leakage methods are good for detecting corrosion damage inside a pipe. The technique has a limitation, however, in detecting or quantifying small surface-open-area flaws or cracks. In addition, there are concerns as to whether stringer-like internal inclusions that are assumed benign could still give a false alarm for any of the inspection systems.

* Corresponding author. Tel.: +1-814-863-8026; fax: +1-814-863-8164.
E-mail address: jlresm@engr.psu.edu (J.L. Rose).

0020-7683/03/$ - see front matter © 2003 Elsevier Science Ltd. All rights reserved.
doi:10.1016/S0020-7683(03)00097-0

Over the last two decades, ultrasonic guided waves have demonstrated the potential for detecting many defects that occur in tube, pipe or plate structures that are not easily and efficiently detected by other means (Achenbach, 1984; Rose, 1999; Fortunko et al., 1982; Rose et al., 1994; Alleyne and Cawley, 1997). One major benefit of guided waves is in their rapid global inspection capability. Defect classification and sizing with guided waves, however is still an important issue to be resolved in order for this technique to be more useful than just a defect screening method. Many researchers have tried to tackle guided wave scattering problems using various methods, e.g. Alleyne and Cawley (1992) studied the interaction of Lamb waves with notches of various depth, width and angle with respect to the normal of the plate surface by using a purely time domain finite element method (FEM) combined with 2-D Fourier transform; Valle et al. (2001) examined the Lamb wave propagation in a hollow isotropic cylinder wall containing a crack with a commercial FEM software package and a time–frequency signal processing technique. Chang and Mal (1999) and Mal and Chang (2000) studied the scattering of Lamb waves from rivet holes and cracks in plates using hybrid frequency domain FEM and normal mode expansion (called global–local FEM technique) followed by FFT inversion to obtain the scattered field in time domain. Abduljabbar et al. (1983) studied the diffraction of horizontal shear waves by normal edge cracks in a plate; Karim et al. (1992) studied the Lamb wave scattering from cracks and inclusions in a plate due to a vertical Gaussian beam load with a hybrid FEM and normal function expansion method. Liu and Datta (1993) also calculated the surface displacements when a steel ball impacts on a plate with cracks using a hybrid FEM at the near field and a boundary integral representation at the far field. Some additional work can be found in Paffenholz et al. (1990), Liu et al. (1991) and Karunasena et al. (1991).

Recently, the boundary element method (BEM) has shown many advantages in wave scattering problems, such as reduction of dimensionality, computational efficiency in less computer time and storage, easy management of unbounded domains and more targeted calculations (Brebbia et al., 1984; Schafbuch et al., 1990). A hybrid BEM combined with the normal mode expansion technique has been used to study Lamb wave mode conversion from the edge of a plate (Cho and Rose, 1996) and its interaction with surface breaking defects (Rose et al., 2000; Cho and Rose, 2000). Our initial work on SH wave sizing potential was reported in Rose and Zhao (2001), where the same technique was extended to study the interaction of the n_0 mode SH wave with various crack and corrosion boundaries in a structure. For stringer-like internal inclusions, Rokhlin (1980, 1981) did some studies on the diffraction and resonance phenomena of Lamb waves by a finite parallel crack in a plate using Wiener-Hopf technique and multiple diffraction methods. The reflection and transmission characteristics of Lamb and SH waves impinging onto a stringer inclusion was not yet presented in the literature.

In this paper, the hybrid BEM normal mode expansion technique is applied to the study of both Lamb and SH waves of any mode of incidence onto a half-elliptical shaped surface breaking defect of three different opening lengths (0.3, 6.35 and 12.7 mm) and of various depths (10%, 30%, ..., 90% through-wall depth). Attempts were made to find the best mode and frequency with the best chance of success in carrying out the defect classification and sizing study. A stringer-like internal inclusion in a plate was also modeled and studied in order to examine its effect on the propagation of guided waves. It turned out that the S_0 mode Lamb wave and the n_0 mode SH wave at low frequencies had a monotonic increase in their reflected signal amplitudes and a decrease in transmitted signal amplitudes with an increase of defect through-wall depth for all three surface breaking defects. This is potentially a breakthrough result in simplifying sizing algorithms significantly provided the right frequency range is used. When frequency increases, more modes will propagate in the structure due to mode conversion at the defect boundary. The wave energy is redistributed. The monotonic trend does not hold any longer except for some sporadic frequency ranges. The stringer-like internal inclusions did not generate much interference for the n_0 mode SH wave for most of the frequencies and the S_0 mode Lamb wave below the first cut-off frequency (the A_1 mode cut-off). Most of the wave energy passed through the inclusion region with little reflection. Higher order mode SH waves, high frequency S_0 and other mode Lamb waves would certainly "see" the inclusion. For the experiments,

the three half-elliptical shaped surface breaking defects were fabricated in 10 mm thick steel plates. Lamb waves were generated and received by a piezoelectric transducer mounted on a variable angle Plexiglas wedge and the SH waves were generated by periodical permanent magnets (PPM) EMATs. Reflected and transmitted time domain signal amplitudes were recorded to calculate the reflection and transmission coefficients. They agreed quite well with the BEM results.

2. Hybrid boundary element-normal mode expansion solutions

The study was carried out on half-elliptical shaped scatterers with variations in defect depth and opening length values as shown in Fig. 1. The thin stringer-like internal inclusion studied is shown in Fig. 2. An incident time harmonic wave is considered propagating in the positive x_1 direction. The mode incident onto the defects results in both reflected and transmitted waves of all orders of the propagating as well as non-propagating modes in the vicinity of the crack. The evanescent modes die out quickly within several wavelengths, thus only propagating modes can exist and carry energy flux in the plate far away from the defect (Koshiba et al., 1984; Vasudevan and Mal, 1985). The hybrid boundary element normal mode expansion technique works in a way that at the far field of the scattered waves, the total displacement and traction are the superposition of all of the incident and scattered propagating wave fields, i.e.,

$$U(x_1,x_2)=\begin{cases} A_p^{\mathrm{IN}}U^p(x_2)\mathrm{e}^{\mathrm{i}k_px_1}+\sum_{n=0}^{\infty}A_n^-U^n(x_2)\mathrm{e}^{-\mathrm{i}k_nx_1}; & (x_1\leqslant\Gamma_-),\\ \sum_{n=0}^{\infty}A_n^+U^n(x_2)\mathrm{e}^{+\mathrm{i}k_nx_1}; & (x_1\geqslant\Gamma_+),\end{cases} \tag{1}$$

$$T(x_1,x_2)=\begin{cases} A_p^{\mathrm{IN}}T^p(x_2)\mathrm{e}^{\mathrm{i}k_px_1}+\sum_{n=0}^{\infty}A_n^-T^n(x_2)\mathrm{e}^{-\mathrm{i}k_nx_1}; & (x_1\leqslant\Gamma_-),\\ \sum_{n=0}^{\infty}A_n^+T^n(x_2)\mathrm{e}^{+\mathrm{i}k_nx_1}; & (x_1\geqslant\Gamma_+),\end{cases} \tag{2}$$

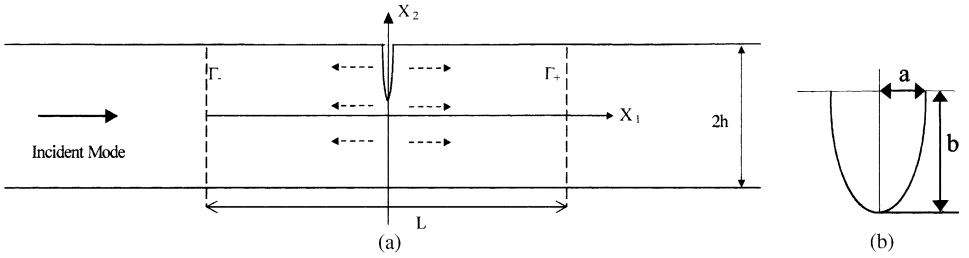

Fig. 1. (a) Sketch for the wave scattering analysis. Solid and dashed arrows show incident and scattered modes respectively. Area contained between $\Gamma_\pm$ lines is used for BEM modeling. L is larger than two wavelengths. (b) Parameters for the elliptical shape defect.

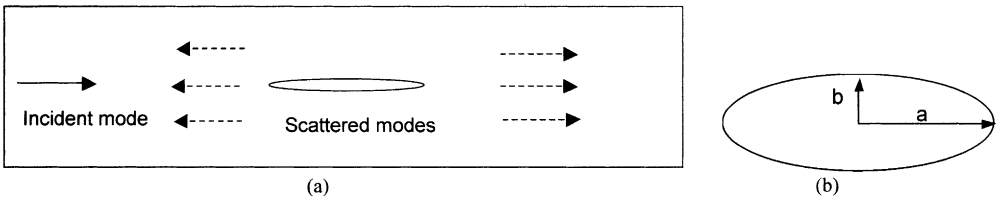

Fig. 2. (a) Problem statement and (b) void geometry for SH wave scattering from the elliptical void in a plate.

where A_p^{IN} is the known amplitude of the incident pth mode, $A_n^{\pm}$ denotes the unknown amplitudes of the scattered waves traveling in the positive and negative x_1 directions respectively. $U^n(x_2)$ and $T^n(x_2)$ denote the known normalized displacement and traction model functions of the nth mode in the plate, respectively. k_n represents the wave number. The time dependent term $e^{-i\omega t}$ is omitted elsewhere.

At the region where there is a defect, the BEM was used to calculate the wave field due to irregular boundary geometry. The boundary value problem modeling the region with defects leads to the following boundary integral equations:

For Lamb waves:

$$C_{ki}(\vec{\xi})u_i(\vec{\xi}) + \int_\Gamma t_{ki}^*(\vec{\xi},\vec{\chi})u_i\,\mathrm{d}\Gamma = \int_\Gamma u_{ki}^*(\vec{\xi},\vec{\chi})t_i\,\mathrm{d}\Gamma. \tag{3}$$

For SH waves:

$$C(\vec{\xi})u(\vec{\xi}) + \int_\Gamma \frac{\partial u^*(\vec{\xi},\vec{\chi})}{\partial n}u(\vec{\chi})\,\mathrm{d}\Gamma(\vec{\chi}) = \int_\Gamma u^*(\vec{\xi},\vec{\chi})\frac{\partial u(\vec{\chi})}{\partial n}\,\mathrm{d}\Gamma(\vec{\chi}). \tag{4}$$

Here Γ is the total boundary of the modeling area. $\vec{\xi}$ is a position vector of the unit point source load and $\vec{\chi}$ is a field point. The values of $C_{ki}(\xi)$ and $C(\xi)$ depend on boundary smoothness. They are equal to 1/2 if Γ is smooth, $\partial u/\partial n$ is the derivative of u with respect to the outward normal to the boundary Γ. $u_i(\vec{\chi})$, $u(\vec{\chi})$ are the displacements on the boundary and t_{ki} and $\partial u/\partial n$ are the tractions. The terms $u_{ki}^*(r)$, $u^*(r)$ and $t_{ki}^*(r)$ refer to the fundamental solutions in frequency domain. For example, $u^*(r)$ can be expressed as a Hankel function of the first kind (Kobayashi, 1987)

$$u^*(r) = \frac{\mathrm{i}}{4}H_0^{(1)}\left(\frac{\omega}{c_{\mathrm{T}}}r\right), \tag{5}$$

and $u_{ki}^*(r)$ and $t_{ki}^*(r)$ expressed as

$$u_{ki}^*(\xi,\chi) = A(\widehat{U}_1\delta_{ki} - \widehat{U}_2 r_{,k}r_{,i}), \tag{6}$$

$$\begin{aligned} t_{ki}^*(\xi,\chi) = GA\Bigg[&\left\{\left(\delta_{ki}\frac{\partial r}{\partial n} + n_i r_{,k}\right) + \frac{\lambda}{G} + n_i r_{,k}\right\}\frac{\mathrm{d}\widehat{U}_1}{\mathrm{d}r} - \left\{\left(\delta_{ki}\frac{\partial r}{\partial n} + n_i r_{,k}\right)\right. \\ &\left. + 2\left(n_{,i}r_{,k} - 2r_{,k}r_{,i}\frac{\partial r}{\partial n}\right) + \alpha\frac{\lambda}{G}n_i r_{,k}\right\}\frac{\widehat{U}_2}{r} - \left\{2r_{,k}r_{,i}\frac{\partial r}{\partial n} + \frac{\lambda}{G}n_i r_{,k}\right\}\frac{\mathrm{d}\widehat{U}_2}{\mathrm{d}r}\Bigg], \end{aligned} \tag{7}$$

where the distance between a unit point source and field point r and coefficients α and A are defined as $r(\vec{\xi},\vec{\chi}) = |\vec{\xi} - \vec{\chi}|$, $\alpha = 1$ and $A = \mathrm{i}/4G$ for the 2-D case. $\widehat{U}_1$, $\widehat{U}_2$ in Eqs. (6) and (7) are

$$\widehat{U}_1 = H_0^{(1)}(k_{\mathrm{T}}r) - \frac{1}{k_{\mathrm{T}}r}H_1^{(1)}(k_{\mathrm{T}}r) + \left(\frac{k_{\mathrm{L}}}{k_{\mathrm{T}}}\right)^2 H_1^{(1)}(k_{\mathrm{L}}r), \tag{8}$$

$$\widehat{U}_2 = -H_2^{(1)}(k_{\mathrm{T}}r) + \left(\frac{k_{\mathrm{L}}}{k_{\mathrm{T}}}\right)^2 H_2^{(1)}(k_{\mathrm{L}}r), \tag{9}$$

where k_{L} is the longitudinal wave number, k_{T} is the transverse wave number and $H_0^{(1)}$, $H_1^{(1)}$ and $H_2^{(1)}$ are the Hankel functions of the first kind of order 0, 1 and 2.

By discretizing the domain boundary into N constant boundary elements, Eqs. (3) and (4) can be transformed into

$$c^i\mathbf{u}^i + \sum_{j=1}^{N}\left\{\int_{\Gamma_j}\mathbf{t}^*\,\mathrm{d}\Gamma\right\}\mathbf{u}^j = \sum_{j=1}^{N}\left\{\int_{\Gamma_j}\mathbf{u}^*\,\mathrm{d}\Gamma\right\}\mathbf{t}^j, \tag{10}$$

noting that $\mathbf{u}^j$ and $\mathbf{t}^j$ are constant on the jth element Γ_j and are taken out of the integral. Here vector notion is used, i.e.

For Lamb waves

$$\mathbf{u} = \begin{bmatrix} u_1 \\ u_2 \end{bmatrix}; \quad \mathbf{t} = \begin{bmatrix} t_1 \\ t_2 \end{bmatrix}; \quad \mathbf{u}^* = \begin{bmatrix} u_{11}^* & u_{12}^* \\ u_{21}^* & u_{22}^* \end{bmatrix}; \quad \mathbf{t}^* = \begin{bmatrix} t_{11}^* & t_{12}^* \\ t_{21}^* & t_{22}^* \end{bmatrix}. \tag{11}$$

For SH waves

$$\mathbf{u} = u_3; \quad \mathbf{t} = \partial u_3/\partial n; \quad \mathbf{u}^* = u_3^*; \quad \mathbf{t}^* = \partial u_3^*/\partial n. \tag{12}$$

By defining

$$G^{ij} = \int_{\Gamma_j}\mathbf{u}^*\,\mathrm{d}\Gamma, \quad \widehat{H}^{ij} = \int_{\Gamma_j}\mathbf{t}^*\,\mathrm{d}\Gamma \quad \text{and} \quad H^{ij} = \begin{cases} \widehat{H}^{ij} & \text{when} \quad i \neq j \\ \widehat{H}^{ij} + c^i & \text{when} \quad i = j \end{cases} \tag{13}$$

Eq. (10) can be rewritten as

$$\sum_{j=1}^{N} H^{ij}\mathbf{u}^j = \sum_{j=1}^{N} G^{ij}\mathbf{t}^j \tag{14}$$

or in a matrix form

$$\mathbf{HU} = \mathbf{GT} \quad \text{on } \Gamma, \tag{15}$$

where **U** and **T** are the total boundary displacement and traction vectors. **H** and **G** are the boundary integral terms of the traction and displacement of the fundamental solutions.

Now consider the mesh geometry between Γ_- and Γ_+ as shown in Fig. 1. By separating the boundary elements into four groups "Top", "Γ_-", "Bot" and "Γ_+", which stands for the elements on the top surface, left virtual boundary, bottom surface and right virtual boundary, respectively, Eq. (15) can be written as:

$$[\mathbf{H}]\begin{bmatrix} \mathbf{u}_{\mathrm{Top}} \\ \mathbf{u}_{\Gamma_-} \\ \mathbf{u}_{\mathrm{Bot}} \\ \mathbf{u}_{\Gamma_+} \end{bmatrix} = [\mathbf{G}]\begin{bmatrix} 0 \\ \mathbf{t}_{\Gamma_-} \\ 0 \\ \mathbf{t}_{\Gamma_+} \end{bmatrix}. \tag{16}$$

Here the traction free boundary conditions are already implemented in the equations. The only non-zero traction term is from the virtual boundaries, where the incident wave and scattered waves superimpose.

Note that in Eqs. (1) and (2), A_p^{IN} and $A_n^{\pm}$ are the same in the both the expansions of the displacement and traction fields, thus they can be eliminated, and $\mathbf{t}_{\Gamma_\pm}$ can be expressed as an explicit linear function of $\mathbf{u}_{\Gamma_\pm}$. For example, on the left virtual boundary, the SH wave displacement and tractions are

$$\{u\}_{k\times 1}^{\Gamma_-} = [\bar{\boldsymbol{u}}]_{k\times J}^{\mathrm{IN}}\{A_p^{\mathrm{IN}}\delta_{pj}\mathrm{e}^{\mathrm{i}kj_{x1}}\}_{J\times 1} + [\bar{\boldsymbol{u}}]_{k\times J}^{\mathrm{BS}}\{A_j^{-}\mathrm{e}^{-\mathrm{i}kj_{x1}}\}_{J\times 1} \quad \text{on } \Gamma_-, \tag{17}$$

$$\{t\}_{k\times 1}^{\Gamma_-} = [\bar{\boldsymbol{t}}]_{k\times J}^{\mathrm{IN}}\{A_p^{\mathrm{IN}}\delta_{pj}\mathrm{e}^{\mathrm{i}kj_{x1}}\}_{J\times 1} + [\bar{\boldsymbol{t}}]_{k\times J}^{\mathrm{BS}}\{A_j^{-}\mathrm{e}^{-\mathrm{i}kj_{x1}}\}_{J\times 1} \quad \text{on } \Gamma_-, \tag{18}$$

where k elements are assumed on Γ_- and there are J modes of SH waves in the plate. The terms $[\bar{\boldsymbol{u}}]_{k\times J}^{\mathrm{IN}}$ and $[\bar{\boldsymbol{u}}]_{k\times J}^{\mathrm{BS}}$ are the normalized incident and scattered displacement model matrices, respectively, $[\bar{\boldsymbol{t}}]_{k\times J}^{\mathrm{IN}}$ and $[\bar{\boldsymbol{t}}]_{k\times J}^{\mathrm{BS}}$ are the corresponding traction matrices. From Eq. (17), the scattered wave model amplitude is

$$\{A_j^- e^{-ikj_{x1}}\}_{J\times 1} = [\bar{u}^{-1}]^{BS}_{J\times k}\{u\}^{\Gamma_-}_{k\times 1} - [\bar{u}^{-1}]^{BS}_{J\times k}[\bar{u}]^{IN}_{k\times J}\{A_p^{IN}\delta_{pj}e^{ikj_{x1}}\}_{J\times 1} \quad \text{on } \Gamma_-. \tag{19}$$

By substituting Eq. (19) into Eq. (18),

$$\{t\}^{\Gamma_-}_{k\times 1} = ([\bar{t}]^{IN}_{k\times J} - [\bar{t}]^{BS}_{k\times J}[\bar{u}^{-1}]^{BS}_{k\times J}[\bar{u}]^{IN}_{k\times J})\{A_p^{IN}\delta_{pj}e^{ikj_{x1}}\}_{J\times 1} + [\bar{t}]^{BS}_{k\times J}[\bar{u}^{-1}]^{BS}_{k\times J}\{u\}^{\Gamma_-}_{k\times 1} \quad \text{on } \Gamma_- \tag{20}$$

i.e. $\mathbf{t}_{\Gamma_-}$ is expressed as a linear function of $\mathbf{u}_{\Gamma_-}$.

Similarly, $\mathbf{t}_{\Gamma_+}$ can be expressed by $\mathbf{u}_{\Gamma_+}$ and thus Eq. (16) will provide us with a unique solution of the boundary values of the total displacement field of the SH waves. Consequently, the unknown backward and forward scattered SH wave mode amplitudes can be determined through Eq. (19) etc., and the nth mode reflection coefficient $|R|_{np}$ and transmission coefficient $|T|_{np}$ can be calculated by dividing the scattered mode amplitude to the incident pth mode amplitude, i.e.

$$|R|_{np} = A_n^-/A_p^{IN}; \quad |T|_{np} = A_n^+/A_p^{IN}. \tag{21}$$

For Lamb waves, the same procedure also applies except that the displacement and traction field will have two components for each boundary element instead of just one as in the SH wave case. Detailed formula derivations can be found in (Cho and Rose, 2000) and will not be iterated here.

3. BEM calculation on surface breaking defects

Two-dimensional BEM Fortran codes were developed for calculating the reflection and transmission coefficients of both Lamb and SH waves on a plate with arbitrary shaped defects (Zhao et al., 2002). The results presented here were used for a sizing study of elliptical defects of 10%, 30%, ..., 90% through plate thicknesses with opening lengths $2a$ equal to 0.3, 6.35 or 12.7 mm on 10 mm steel plates (see Fig. 3). Code accuracy was proven through benchmark comparison studies (Cho and Rose, 1996). The boundary element size was chosen to be less than one fifteenth of the shear wavelength, which proved to be sufficient for computation convergence. The length of the meshed region was chosen to be at least ten times the plate thickness in order to neglect the evanescent modes. The material properties for steel were chosen as: longitudinal wave velocity $c_L = 5.9$ mm/μs, the transverse wave velocity $c_T = 3.2$ mm/μs and density $\rho = 7.8$ g/cm^3. Fig. 4 shows the phase and group velocity dispersion curves for Lamb waves in a 10 mm steel plate. The lowest three wave modes are marked on the figure and the first cut-off frequency is seen around 200 kHz. Notice that at a given frequency point, at least two wave modes could possibly propagate in a plate. All of these normal modes have different wave structure and wave numbers. The scattered wave field is

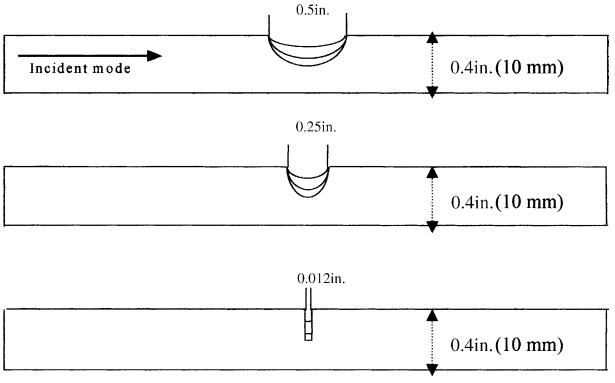

Fig. 3. Modeling statement of a guided wave striking elliptical defects of 10%, 20%, ..., 90% through plate thickness.

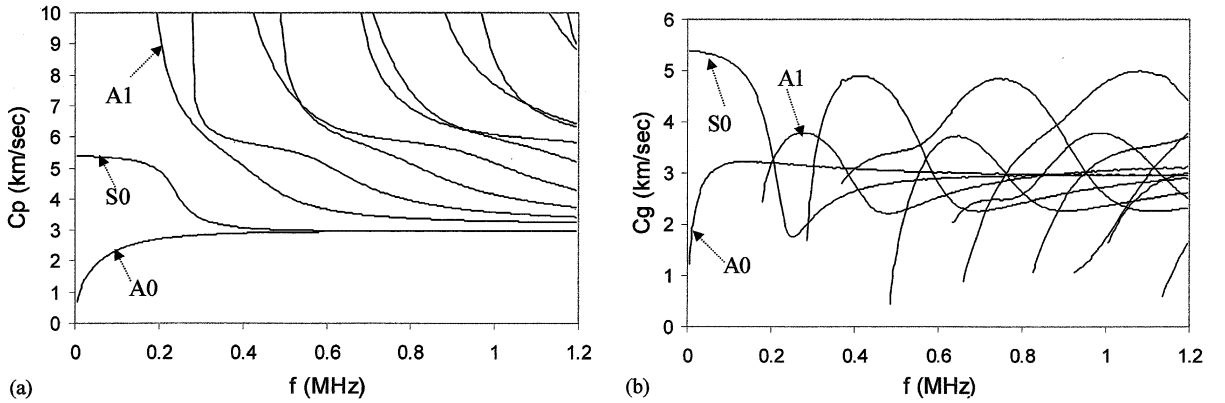

Fig. 4. The Lamb wave dispersion curve for 10 mm steel plate. (a) Phase velocity and (b) group velocity.

constructed in the plate at several wavelengths away from the defects. The BEM calculated reflection and transmission coefficients versus frequency are plotted in Figs. 5–7 for the S_0 mode Lamb wave incident onto the three half-elliptical shaped defects, respectively. They show that the reflection and transmission

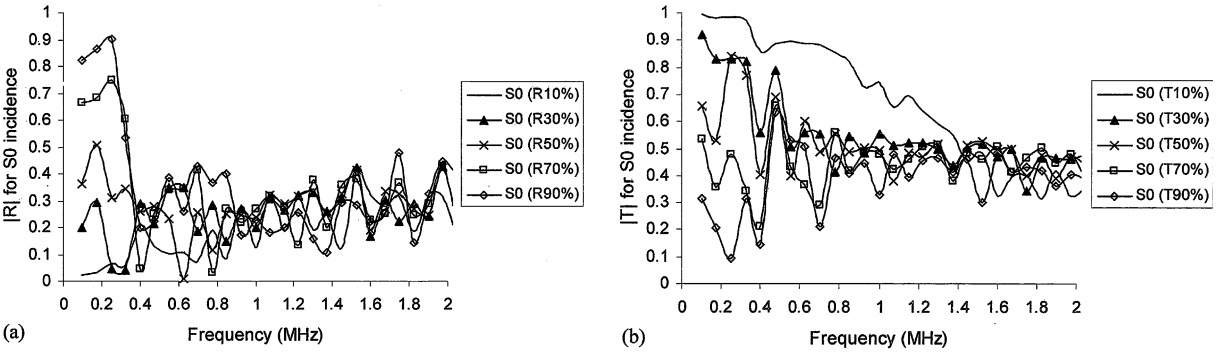

Fig. 5. Calculated (a) reflection and (b) transmission coefficients for S_0 mode under S_0 incident for 0.012 in. (0.3 mm) elliptical defect and 10%, 30%, 50%, 70%, 90% through plate thickness depth.

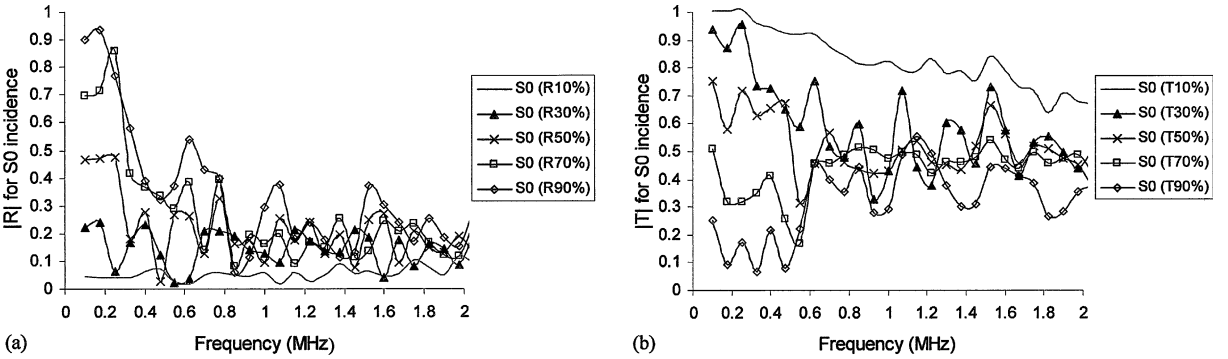

Fig. 6. (a) Approximate reflection and (b) transmission coefficients for S_0 mode under S_0 incident for 0.25 in. (6.35 mm) elliptical defect and 10%, 30%, 50%, 70%, 90% through plate thickness depth.

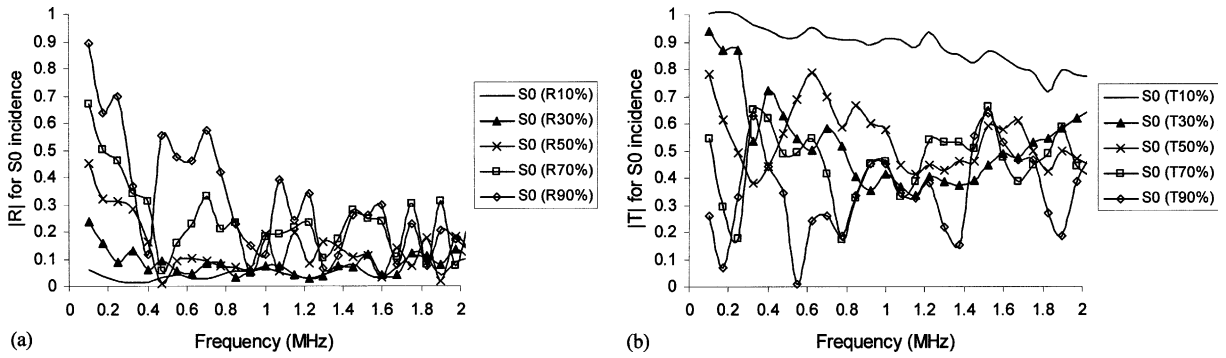

Fig. 7. (a) Approximate reflection and (b) transmission coefficients for S_0 mode under S_0 incident for 0.5 in. (12.7 mm) elliptical defect and 10%, 30%, 50%, 70%, 90% through plate thickness depth.

coefficients of the S_0 mode; Lamb wave are strongly dependent on frequency. They do not increase or decrease monotonically with an increase of defect depth at high frequencies. This phenomenon was also observed for the A_1 mode Lamb wave by Alleyne and Cawley (1992) in their experiments. At low frequencies (e.g. below 200 kHz), however, it can be seen that the reflected S_0 mode signal amplitude increases monotonically, and the transmitted S_0 mode signal amplitude decreases monotonically, with the percentage through-wall defect depth increase for all three types of surface opening defects. Calculations were also conducted for the A_0 mode Lamb wave, but no such properties were observed at low frequencies.

Intuitively, this monotonic trend of amplitude change is due to the fact that the in-plane displacement and stress field of the S_0 mode at low frequencies are dominant, and they are relatively uniform throughout the plate thickness. The wave energy reflected from and transmitted through the defect region thus changes monotonically with the defect depth, as long as the defect length (in the wave propagation direction) is small compared to the wavelength of that mode.

Similar calculations were also conducted for the SH wave n_0, n_1 and n_2 modes. Fig. 8(a) and (b) show the phase and group velocities of the SH waves in a 10 mm steel plate. The lowest order mode n_0 and also n_1 are marked. Fig. 9 shows the reflection and transmission coefficients versus frequency for the SH n_0 mode wave incident onto the 0.3 mm notch defect. An excellent monotonic increase in reflection coefficient amplitude and decrease in transmission coefficient amplitude are seen with an increase of the defects' percentage through-wall depths for most frequencies. Those coefficients do not vary much at higher frequencies. This

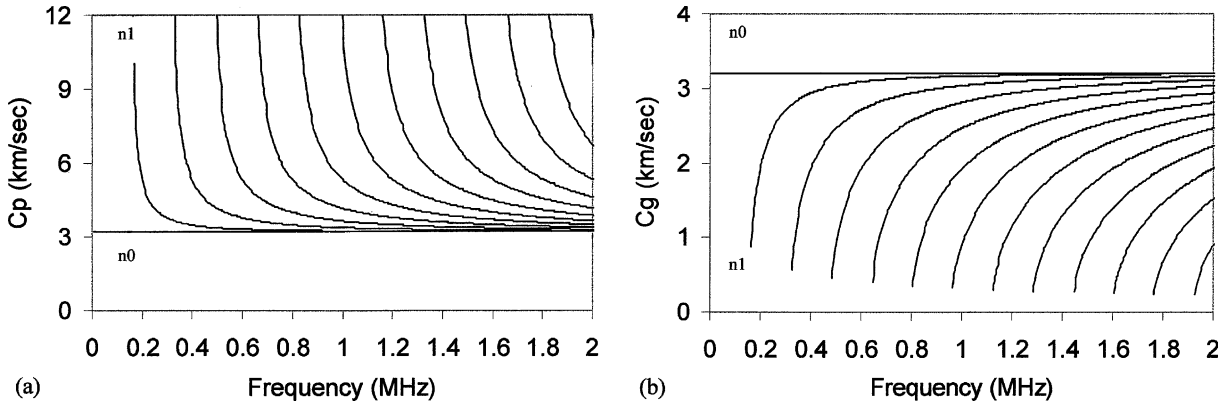

Fig. 8. The shear horizontal wave dispersion curve for a 10 mm steel plate. (a) Phase velocity and (b) group velocity.

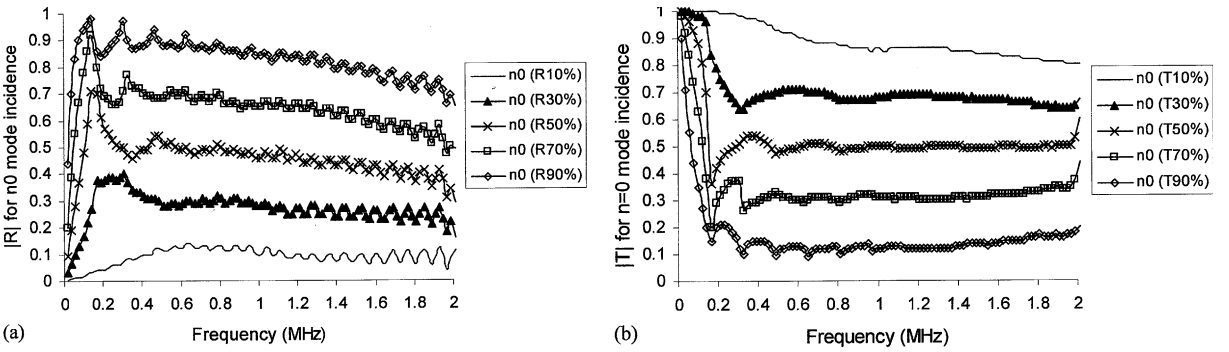

Fig. 9. (a) Approximate reflection and (b) transmission coefficients for n_0 mode under n_0 incident for 0.012 in. (0.3 mm) elliptical defect length and 10%, 30%, ..., 90% through plate thickness depth.

phenomenon may again be explained by the uniformity of the displacement and stress field of the n_0 mode throughout the plate thickness. Monotonic trends were also obtained for 6.35 and 12.7 mm defects at low frequencies as shown in Figs. 10 and 11. The transmission coefficients continue to observe the monotonic

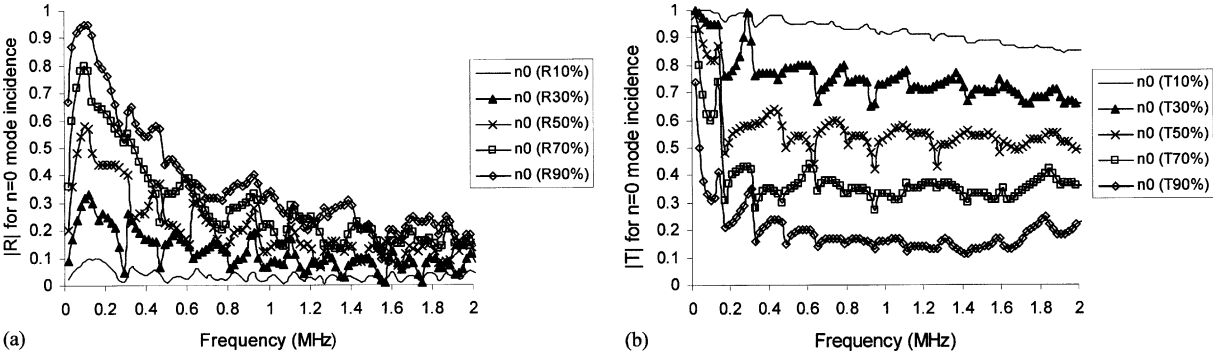

Fig. 10. (a) Approximate reflection and (b) transmission coefficients for n_0 mode under n_0 incident for 0.25 in. (6.35 mm) elliptical defect length and 10%, 30%, ..., 90% through plate thickness depth.

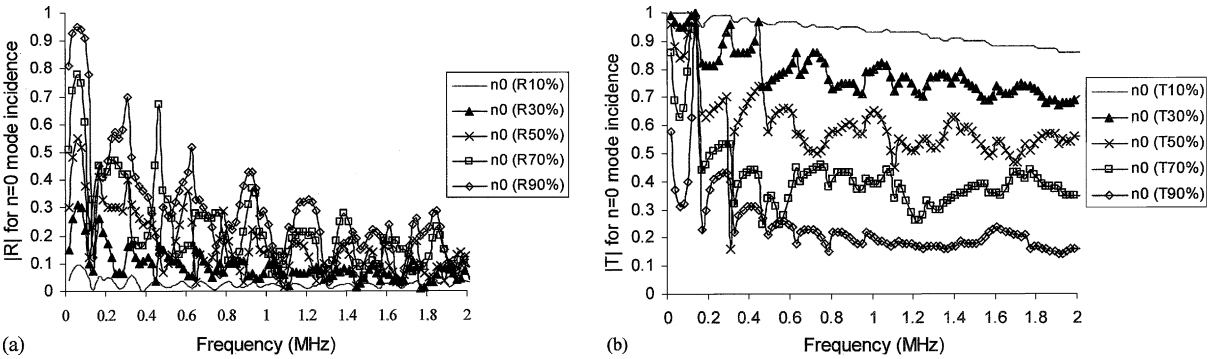

Fig. 11. (a) Approximate reflection and (b) transmission coefficients for n_0 mode under n_0 incident for 0.5 in. (12.7 mm) elliptical defect length and 10%, 30%, ..., 90% through plate thickness depth.

trend for most of the frequencies. However, the reflection coefficients become frequency sensitive and the monotonic trend may not hold for frequencies above 300 kHz. This might be due to the phase variation of the waves reflecting from a curved surface (elliptical in this case). Also note in Fig. 9(a) and (b), that there are local peaks and valleys on the 90% defect reflection and transmission curves. Compared with the dispersion curves for SH waves, it is seen that these local extremes appeared at the cut-off frequencies. More studies will be conducted on this resonance effect.

4. BEM calculation on internal inclusions

It appears that the low frequency S_0 mode Lamb and n_0 mode SH waves would have great potential in defect through-wall depth sizing, yet there is a concern as to whether a benign stringer like an internal inclusion (e.g. a void) in a plate would indicate a false alarm. To answer this question, BEM calculations were conducted on a 10 mm thick steel plate with a 50 mm long, 0.3 mm wide internal elliptical inclusion at the mid-plane of the plate (Fig. 2). Reflection and transmission coefficients for the S_0 mode Lamb wave and n_0 mode SH wave incidence versus frequency were calculated respectively. Fig. 12(a) and (b) shows the reflection and transmission coefficients of the S_0, S_1, S_2, A_0 and A_1 modes versus frequency for the S_0 mode Lamb wave incidence, while Fig. 13(a) and (b) shows those of the n_0, n_1 n_2, n_3 and n_4 mode SH waves for n_0

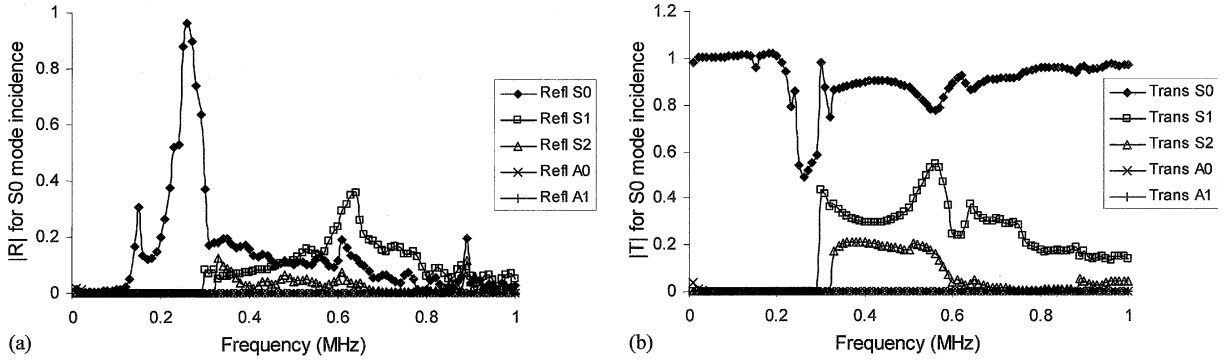

Fig. 12. (a) Reflection and (b) transmission coefficients of the S_0, S_1, S_2, A_0, A_1 mode Lamb waves versus frequency for a 50 mm long, 0.3 mm wide internal elliptical inclusion in a 10 mm thick steel plate with S_0 mode incidence.

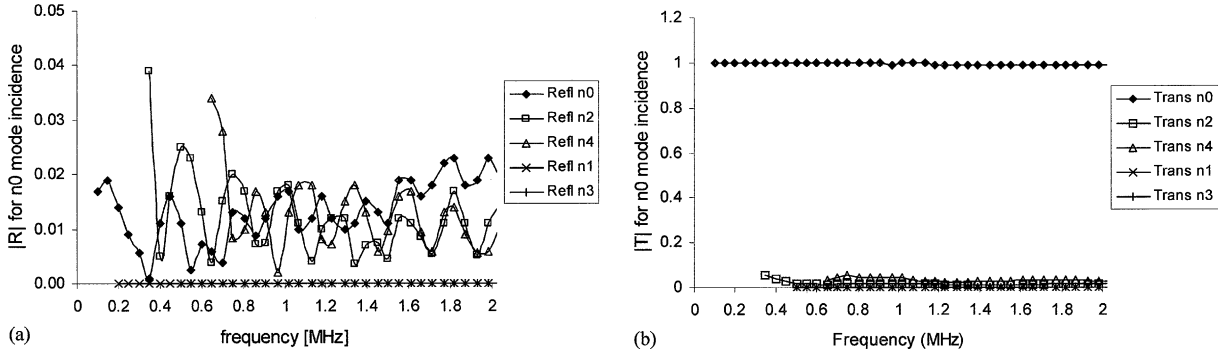

Fig. 13. (a) Reflection and (b) transmission coefficients of the n_0, n_1, n_2, n_3 and n_4 mode SH waves versus frequency for a 6 mm long, 0.2 mm wide internal elliptical inclusion with the n_0 mode incidence.

mode incidence. Note that in these two figures, the inclusion of S_1, S_2, A_0, A_1 and n_1, n_2, n_3 and n_4 modes is to show the effect of mode conversion due to the defect.

It is shown that the low frequency (below the first cut-off frequency) S_0 mode Lamb wave and the n_0 mode SH wave energy over most frequencies will pass through the inclusion region with almost no reflection. There is no mode conversion from a symmetric mode to an anti-symmetric mode for both the Lamb wave and SH waves for all frequencies, thus both the reflection and transmission coefficients of the A_0, A_1 mode Lamb wave and n_1, n_3 mode SH wave are zero, as is seen from the figures. When the incident frequency goes beyond the first cut-off frequency, however, both the S_0 mode Lamb wave and the mode converted higher order symmetric modes would be reflected back, and thus would be able to see the stringer.

5. Experimental setup and data collection

Experiments on defect through-wall sizing were conducted on sixteen 10 mm thick steel plates. Fifteen of the plates were approximately 450 mm long and 200 mm wide, each having a 0.3, 6.35 or 12.7 mm long and 10%, 30%, 50%, 70% or 90% through-wall half-elliptical defect in it. The other plate was approximately 550 mm long and 130 mm wide. It had an EDM machined 0.3 mm wide, 50 mm long and through-plate internal inclusion in the mid-plane. Two piezoelectric transducers of center frequency 175 kHz and bandwidth from 130 to 220 kHz were mounted on 30° angle Plexiglas wedges. They were used to generate and receive the S_0 mode Lamb wave in a plate in utilizing Snell's law for a conversion to phase velocity. The n_0 mode SH wave was generated and received by two SH wave PPM EMATs at a center frequency of 210 kHz. The experiment makes use of a Matec Explorer II system which has a high power tone burst card for generating rectangular windowed sinusoidal waveforms, and a DSP board for receiving and digital processing signals for filtering and amplification. The waveforms can be displayed on the screen and stored for further analysis. In the experiment, time domain signal peak-to-peak amplitudes were measured for calculating the reflection and transmission coefficients at the center frequency of the tone burst signal. This approximation is valid as long as the signal has a fairly narrow bandwidth. A more accurate calculation might require a Fourier transform of the time domain signal in moving to frequency domain, hence calculating the coefficients for individual frequency points. During the transmission coefficients measurement, a reference signal was obtained first by separating two transducers (piezoelectric transducers for the Lamb wave measurement and SH EMATs for the SH waves) 150 mm apart on the clean part of a plate with no defect in between. The signal amplitude was recorded. The transducers were then placed on the plate with a defect in between with each transducer approximately 75 mm away from the center of the defect. The transmitted signal amplitude was thus recorded. Care should be taken for the edge reflection from the plate end when using the PPM EMAT since it generates and receives waves bi-directionally. For the reflection coefficients measurement, a simulated pulse-echo reference signal was obtained first by facing the two transducers at an angle (about 15° to the edge normal) to the plate edge to compensate for beam divergence. The reflected signals from the defects were then recorded with the same transducer setup. Finally, the peak-to-peak values of the reflected and transmitted signals were divided by the corresponding reference signal to give the reflection and transmission coefficients.

6. Experimental results and discussion

The experimental and BEM-predicted reflection and transmission coefficients are compared in this section for both the Lamb and SH waves impinging onto the surface breaking defects as well as the stringer-like internal inclusion. Comparisons are made at only one frequency point (175 kHz for the S_0 mode Lamb

wave and 210 kHz for the n_0 mode SH wave), and the experimental measured reflection and transmission coefficients are their averaged values around the center frequency point. Reasonable agreement was obtained between the experimental and BEM results. Specifically, Fig. 14(a) and (b) plots the reflection and transmission coefficients of the S_0 mode Lamb wave versus defect percentage through-wall depth for all three types of surface opening half-elliptical defects at 175 kHz. Lines with solid legend markers are the BEM results and the discrete hollow markers show the experimental data. It can be seen that the reflection coefficients for the S_0 mode Lamb wave increase monotonically, and the transmission coefficients decrease monotonically with respect to the percentage through-wall defect depth at 175 kHz for all three types of defects. These coefficients tend not to depend on the defect opening lengths since the opening lengths are small compared to the wave length (see also Alleyne and Cawley, 1992). The monotonic trend of the curves for the theoretical and experimental results agrees quite well, although the experimental data tends to be larger in amplitude compared to the corresponding BEM results.

Fig. 15(a) and (b) show comparisons for the n_0 mode SH wave at 210 kHz for all three types of surface opening defects. It is also seen that the reflection coefficients increase monotonically, and the transmission coefficients decrease monotonically with respect to the percentage through-wall defect depth for all three types of defects. Relatively good agreement between theoretical and experimental results is obtained. For

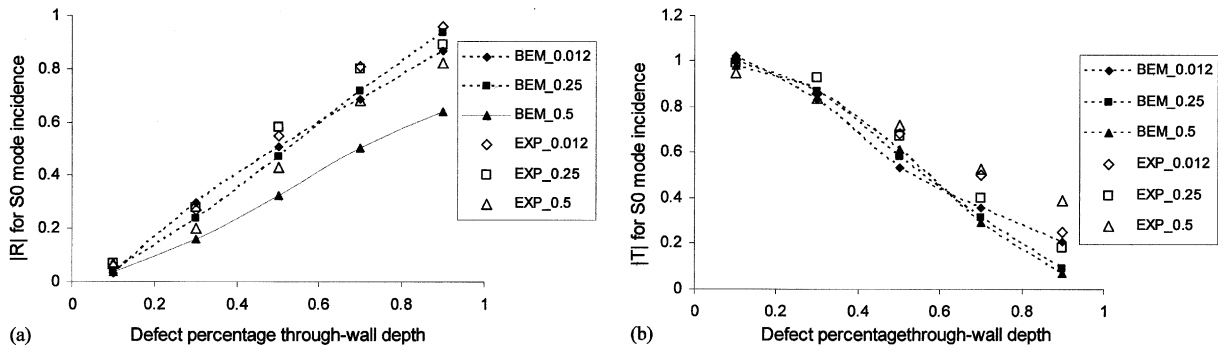

Fig. 14. (a) Approximate reflection and (b) transmission coefficients for S_0 mode under S_0 incident at 175 kHz for 0.012 in. (0.3 mm), 0.25 in. (6.35 mm) and 0.5 in. (12.7 mm) elliptical defect length vs. 10%, 20%, ..., 90% through plate thickness. Lines with solid legend markers are BEM results. Hollow markers are experiment results.

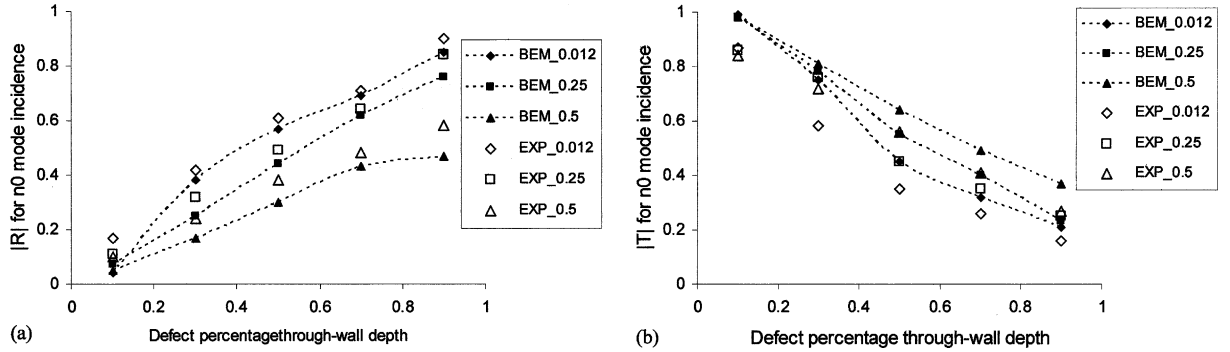

Fig. 15. (a) Approximate reflection and (b) transmission coefficients for n_0 mode under n_0 incident at 210 kHz for 0.012 in. (0.3 mm), 0.25 in. (6.35 mm) and 0.5 in. (12.7 mm) elliptical defect vs. 10%, 20%, ..., 90% through plate thickness. Lines with solid legend markers are BEM results. Hollow markers are experiment results.

the stringer type internal defect, most of the n_0 mode SH wave energy passes through the inclusion region. There is little noticeable signal reflected back, which agrees quite well with the BEM calculations (Fig. 13(a) and (b)). Similar results were also obtained for the S_0 mode Lamb wave at low frequencies.

These results verified the BEM calculations and also eased concerns about the false alarm possibilities from the benign internal stringer inclusions.

7. Conclusion

Defect quantification analysis was carried out for both Lamb and SH guided waves in a plate-like structure. The low frequency S_0 mode Lamb wave and n_0 mode SH wave can be used for through-wall sizing analysis for half-elliptical surface breaking defects somewhat independent of opening lengths for small opening length defects. A monotonic increase in reflection factor and decrease in transmission factor relates to defect through-wall depth increase. Selected frequencies over the range 200 kHz to 2 MHz could also be used for through-wall sizing analysis, but the monotonic amplitude rules may not be in effect. Best results for defect sizing occurs below the first cut-off frequency for both Lamb and SH waves because of less mode conversion. The n_0 mode SH wave could however be considered over the entire frequency range from 0 to 2 MHz. Stringer-like internal inclusions do not affect the detection and sizing of surface breaking defects for the S_0 mode Lamb wave at low frequencies and the n_0 mode SH wave for most frequencies. However, false alarms may be indicated at frequencies above the first cut-off frequency for both Lamb and SH waves. Results presented in this paper are powerful with respect to advancing the state of the art in ultrasonic guided wave inspection. Defect sizing is possible because of the monotonic increase in amplitude observations with defect depth over specific frequency ranges for various mode types.

Acknowledgements

Thanks are given to the Gas Research Institute, Chicago IL for their financial support. Thanks are also given to Dr's Harvey Haines and Al Teitsma for their technical recommendations, Semyen Pelts for some of the BEM code development and Jose Galán for numerical comparison checks.

References

Abduljabbar, Z., Datta, S.K., Shah, A.H., 1983. Diffraction of horizontally polarized shear waves by normal edge cracks in a plate. Journal of Applied Physics 54, 461–472.

Achenbach, J.D., 1984. Wave Propagation in Elastic Solids. Elsevier, New York.

Alleyne, D.N., Cawley, P., 1992. The interaction of lamb wave with defects. IEEE Transaction on Ultrasonics, Ferroelectrics, and Frequency Control 39, 381–397.

Alleyne, D.N., Cawley, P., 1997. Long range propagation of lamb waves in chemical plant pipework. Materials Evaluation 55, 504–508.

Brebbia, C.A., Tells, J.C.F., Wrobel, L.C., 1984. Boundary Element Techniques. Springer, Berlin.

Chang, Z., Mal, A., 1999. Scattering of lamb waves from a rivet hole with edge cracks. Mechanics of Materials 31, 197–204.

Cho, Y., Rose, J.L., 1996. A boundary element solution for a mode conversion study on the edge reflection. The Journal of the Acoustical Society of America 99, 2097–2109.

Cho, Y., Rose, J.L., 2000. An elastodynamic hybrid boundary element study for elastic guided wave interactions with a surface breaking defect. International Journal of Solids and Structures 37, 4103–4124.

Fortunko, C.M., King, R.B., Tan, M., 1982. Nondestructive evaluation of planar defects in plates using low-frequency shear horizontal waves. Journal of Applied Physics 53, 3450–3458.

Karim, M.R., Awal, M.A., Kundu, T., 1992. Elastic wave scattering by cracks and inclusions in plates: in-plane case. International Journal of Solids and Structures 29, 2355–2367.

Karunasena, W., Shah, A., Datta, S., 1991. Plane-strain-wave scattering by cracks in laminated composite plates. Journal of Engineering Mechanics 117, 1738–1754.

Kobayashi, S., 1987. Elastodynamics. In: Boundary Element Methods in Mechanics. North-Holland, Amsterdam, pp. 192–255, Chapter 4.

Koshiba, M., Karakida, S., Suzuki, M., 1984. Finite-element analysis of lamb wave scattering in an elastic plate waveguide. IEEE Transaction on Sonics and Ultrasonics 31, 18–25.

Liu, S., Datta, S., 1993. Scattering of ultrasonic wave by cracks in a plate. Journal of Applied Mechanics 60, 352–357.

Liu, S., Datta, S., Ju, T., 1991. Transient scattering of Raleigh-Lamb waves by a surface-breaking crack: comparison of numerical simulation and experiment. Journal of Nondestructive Evaluation 10, 111–126.

Mal, A.K., Chang, Z., 2000. A semi-numerical method for elastic wave scattering calculations. Geophysical Journal International 143, 328–334.

Paffenholz, J., Fox, J., Gu, X., Jewett, G., Datta, S., Spetzler, H., 1990. Experimental and theoretical study of Rayleigh-Lamb waves in a plate containing a surface-breaking crack. Research in Nondestructive Evaluation 1, 197–217.

Rokhlin, S., 1980. Diffraction of lamb wave by a finite crack in an elastic layer. The Journal of the Acoustical Society of America 67, 1157–1165.

Rokhlin, S., 1981. Resonance phenomena of lamb waves scattering by a finite crack in a solid layer. The Journal of the Acoustical Society of America 69, 922–928.

Rose, J.L., Ditri, J.J., Pilarski, A., Rajana, K., Carr, F.T., 1994. A guided wave inspection technique for nuclear steam generator tubing. NDT & E International 27, 307–330.

Rose, J.L., 1999. Ultrasonic Waves in Solid Media. Cambridge University Press.

Rose, J.L., Pelts, S.P., Cho, Y., 2000. Modeling of flaw sizing potential with guided waves. Journal of Nondestructive Evaluation 19, 55–66.

Rose, J.L., Zhao, X., 2001. Anomaly through-wall depth measurement potential with shear horizontal guided waves. Materials Evaluation 59, 1234–1238.

Schafbuch, P.J., Thompson, R.B., Rizzo, F.J., 1990. Application of the boundary element method to elastic wave scattering by irregular defects. Journal of Nondestructive Evaluation 9, 113–127.

Valle, C., Niethammer, M., Qu, J., Jacobs, L.J., 2001. Crack characterization using guided circumferential waves. The Journal of the Acoustical Society of America 110, 1282–1290.

Vasudevan, N., Mal, A.K., 1985. Response of an elastic plate to localized transient sources. Journal of Applied Mechanics 107, 356–362.

Zhao, X., Rose, J.L., Pelts, S., 2002. Quantitative NDE potential in a wave guide with lamb and shear horizontal waves. Review of Progress in Quantitative Nondestructive Evaluation 21, 196–202.